International Journal of Hydrogen Energy 218 (2026) 154048

Contents lists available at ScienceDirect

International Journal of Hydrogen Energy

journal homepage: www.elsevier.com/locate/he

Distribution of relaxation times-based impedance analysis of incremental PEM water electrolysis cells

Debora Brinker [a,*], Niklas Hensle [a,b], Gözde Kardeş [a], David Breuninger [a], Mika Schächinger [a], August Gladik [a], Philipp Röse [a], André Weber [a]

[a] *Institute for Applied Materials (IAM-ET), Karlsruhe Institute of Technology (KIT), Adenauerring 20b, 76131, Karlsruhe, Germany*
[b] *Fraunhofer Institute for Solar Energy Systems ISE, Heidenhofstrasse 2, 79110, Freiburg, Germany*

ARTICLE INFO

Keywords:
Electrochemical impedance spectroscopy
Distribution of relaxation times
High-pressure testbench
Incremental test cell
High current density
Relaxation frequency

ABSTRACT

We present impedance spectra and related Distribution of Relaxation Times (DRT) analysis of pressurized PEM water electrolysis (PEMWE) single cells obtained with a newly developed test bench, including an incremental (zero-gradient) cell for homogeneous operating conditions. The setup enables reproducible electrochemical impedance spectroscopy (EIS) measurements over technically meaningful operating parameter ranges. DRT analysis reveals that current density variations (0.01–7 A cm^{-2}) show significant issues with the common approach of attributing an electrochemical process to a fixed relaxation frequency. We demonstrate that individual peaks significantly shift their relaxation frequency from the mHz-range at low current densities (0.01 A cm^{-2}) up to the kHz-range at 7 A cm^{-2}. We show variations of current density, temperature, pressure, and water flow rate, which reveal five capacitive and one low-frequency inductive peaks. Our findings emphasize the importance of detailed operating parameter variations for accurately assigning and modeling electrochemical processes in PEMWE cells.

1. Introduction

Electrochemical impedance spectroscopy (EIS) and subsequent distribution of relaxation times (DRT) analysis are valuable tools for thoroughly investigating electrochemical systems, as demonstrated in previous studies on Solid Oxide and PEM fuel cells [1–3]. DRT-based analysis has been introduced into the field of Proton Exchange Membrane Water Electrolysis (PEMWE) in recent years [4–10], focusing on the process assignment and degradation behavior primarily based on variations of current density of up to 2 A cm^{-2}. Relevant higher current densities are not addressed. Additionally, further variations such as cell compression are completely absent. Only Zuo et al. [10] provide a picture of a full frequency range investigation, including the inductive area noticeable at low frequencies, while also operating at current densities up to 2 A cm^{-2}. We ourselves have looked only at the inductive area [11,12] leaving the capacitive region unexplored.

Zuo et al. [9,10] investigate increased gas pressure operation up to 5 bar combined with DRT analysis in two studies. They also mention that further investigations are necessary. For pressure operation testing, a suitable test bench is required. Various testing systems for PEMWE (Proton Exchange Membrane Water Electrolysis) under pressure are already documented in the literature [13–23], with some of them operating in pressure ranges of up to 100 bar [23]. The measurements at these test benches focus on different aspects of the pressure operation. While some examine the total energy consumption [14,20], others focus on the safety aspects of the pressure operation [16,17,23] or on operation and material parameters [13,15,19,21,22]. More detailed investigations of the effect of pressure on current density and the different loss processes are still needed. Garcia-Navarro et al. [24] also showed that many conflicting results are available on the effect of pressure.

Therefore, in this study, we examine the effect of various operation parameters in detail using EIS and DRT analysis techniques. To do this, we introduce our in-house developed test bench and test cell, which can operate under pressure, feature precise temperature control, and allow for water flow rate variations. We present our findings on the functionality of our test bench, demonstrating the stability of our test cells over time and across different samples. Next, we explore parameter variations, including compression force, current density, cathode pressure, temperature, and water flow rate. We provide a detailed analysis of current density variations over a broad range, up to 7 A cm^{-2}, offering

---

* Corresponding author.
E-mail address: debora.brinker@kit.edu (D. Brinker).

https://doi.org/10.1016/j.ijhydene.2026.154048
Received 24 September 2025; Received in revised form 19 January 2026; Accepted 12 February 2026

new insights into behavior at high current densities and changes in relaxation frequency across the current density range. This comprehensive frequency coverage contributes new knowledge to the field. Additionally, we present a cell compression study identifying an optimal compression for our setup. We also provide new results at elevated pressure for high current densities. Finally, we offer an initial assessment of ongoing loss processes.

2. Experimental

To investigate the behavior of PEMWE single cells under pressure, a test bench and test cell capable of operating under these conditions are required. The design of these, the materials used, and the electrochemical characterization method applied in this study are described in the following sections.

2.1. Pressurized test bench

The test bench, shown in Fig. 1, is an in-house developed design for incremental single-cell testing of PEM water electrolysis cells. The incremental (zero gradient) cell can be operated under homogeneous conditions that correspond to local operating states at different positions in an industrial stack. This concept of incremental cell testing is already applied for Solid Oxide Cells [25] as well as PEM fuel cells [2]. For testing PEMWE cells, major adaptations to the PEMFC setup were necessary due to the requirement for pressurized operation and liquid feedwater in the system. Noteworthy features of our test bench include its capacity for high-pressure operation (up to 50 bar) and the ability to mix gases (H_2, O_2, and N_2) into the feed water inlet streams, mimicking gas production of the upstream cell area.

The test bench features two separate water circulation loops, each supplied with deionized (DI) water from a tank positioned at the bottom of the test bench. Micro annular gear pumps (type: mzr-7255-hs-v S by *HNP Mikrosysteme GmbH, Germany*) circulate the water in a flow range of 0.048 mL min^{-1} to 288 mL min^{-1} at both the anode and cathode side and are able to refill water at pressure levels of up to 40 bar. In this study, only the educt water circulation at anode is used. Therefore, the anode must be kept filled with water, and the cathode needs to be drained. To do this, three valves (type: 6027 - Direct-acting 2/2-way plunger valve by *Bürkert GmbH & Co. KG*) are installed in each circulation system, allowing for filling, circulation, and draining modes. To monitor the water level, level sensors (type: CleverLevel® LBFS by *Baumer GmbH*) are used. This enables automatic draining and refilling of the system. Prior to entering the cell, the water is heated via heating cords around the tubes to a desired temperature of up to ~100 °C. The test cell itself can also be heated using heating cartridges, which are controlled separately for the anode and cathode sides. All heaters are individually controlled by PID controllers (type: EUP4420-230VAC-RS by *EG-Tronic GmbH, Germany*), which utilize K-type thermocouple elements for temperature measurement.

The heart of the test bench is the test cell, where the electrochemical conversion occurs. In this study, an in-house developed test cell housing is used, which will be introduced in the next section. The dc-current for the water electrolysis is provided by a galvanostat/potentiostat (introduced in section 2.4). Downstream the cell, the water/gas mixtures are transported to water-gas separators. While the water is recirculated to the cell at the anode side, the oxygen is drained from the system into the ventilation. The water is continuously purified by an ion-exchanger (type: pressure filter MF by *mf microfilter GmbH*). With this, we achieve stable water conductivity values of less than 0.07 μS cm^{-1}, which are continually measured by a conductivity sensor (type: Conducell UPW by *Hamilton Bonaduz AG, Switzerland*) located in the water circulation loop. If the water level drops below a certain level, it will be refilled automatically from the tank. At the cathode side, the water/gas mixture, originating from water that has crossed over through the membrane, is transported via a water/gas separator to a wastewater tank. The produced hydrogen is discharged from the system into the ventilation. Before leaving the system, the product gases can be analyzed with a online-mass spectrometer to check for the amount of gas crossover.

To operate at elevated pressure, a control via pressure controllers (type: EL-PRESS by *Bronkhorst High-Tech B.V., Netherlands*) at the gas outlets is implemented into the test bench. This allows for a pressure operation between ambient pressure and 50 bar. The gases (H_2, O_2, and N_2), which can be introduced into the inlet streams at the anode and cathode side before entering the cell, are controlled by mass flow controllers (EL-FLOW® Prestige by *Bronkhorst High-Tech B.V., Netherlands*). A flow rate of up to 1.6 NL min^{-1} of hydrogen and 0.8 NL min^{-1} of oxygen can be applied to the cathode and anode side, respectively. Nitrogen can be applied to both sides and is used mainly for purging the system. The automation of the test bench is possible by in-house developed software. This enables completely automated testing with the aid of programmable scripts ensuring reproducible repetitions of test procedures.

2.2. Incremental test cell

The in-house developed test cell used in this study is shown in Fig. 2. It has an active area of only 2.1 cm^2 to ensure approximately identical operating conditions throughout the entire active area. Therefore, it is also referred to as an incremental or zero-gradient cell. Such zero-gradient conditions are crucial for enabling the deconvolution of

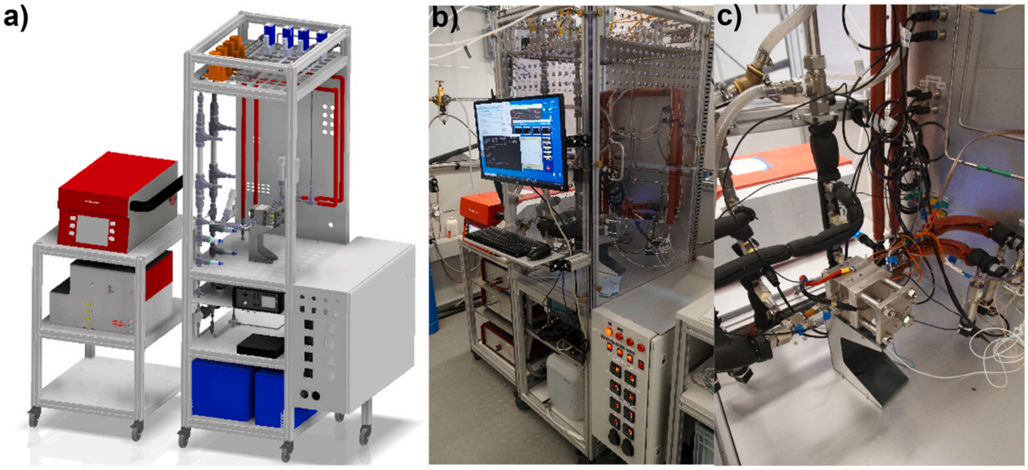

Fig. 1. a) CAD of the test bench created in Autodesk Inventor Professional 2023, b) picture of the whole test bench, and c) picture of the main part of the test bench.

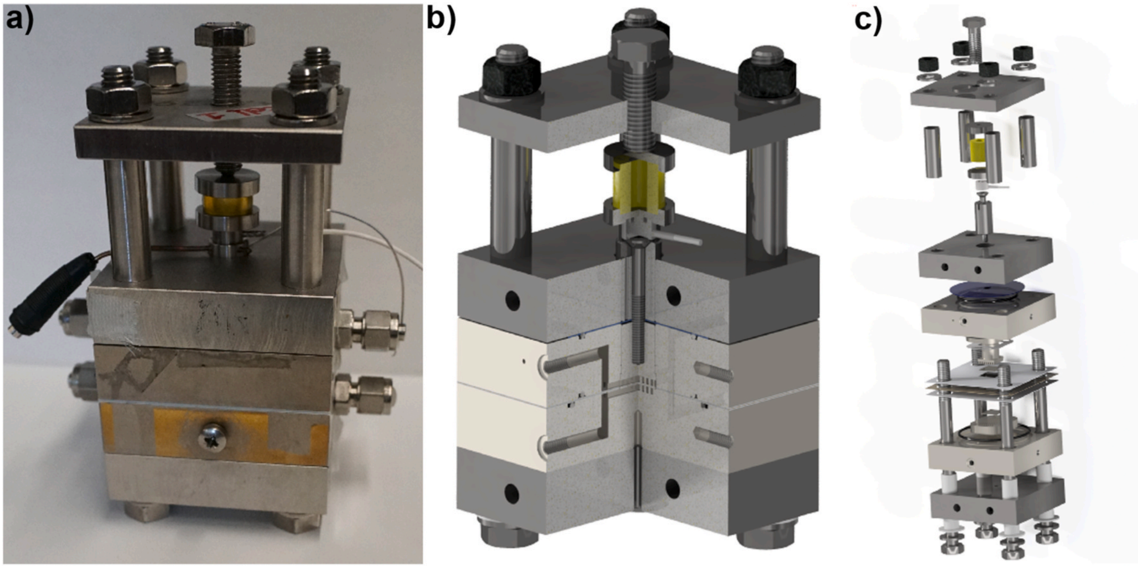

Fig. 2. In-house developed incremental test cell shown as a) picture of assembled test cell, b) three-quarter cut CAD view, and c) explosion view, both created in Autodesk Inventor Professional 2023.

processes with quite similar relaxation frequencies in the DRT.

The cell allows for separate compression of the active area via a stamp construction with an integrated force sensor continuously measuring the applied compression of the active area during operation, as shown in Fig. 2 b). The compression is applied with a screw in the middle of the upper plate, which enables compression changes during testing. Four further screws fasten the outer part of the test cell to keep the cell water and gas tight, also at elevated pressure. The main plates between which the catalyst-coated membrane (CCM) and porous transport layers (PTLs) are placed are made out of titanium. Water, and gas inlets and outlets are positioned on opposite sides of these plates. The flow fields are exchangeable, allowing for the testing of different flow field structures. In this study, we employ a parallel channel design with seven channels with a width of 1 mm and a depth of 2 mm. The land area in between has a width of 0.9 mm. To ensure water and gas tightness up to 50 bar, O-rings combined with flat gaskets are used. The two heating cartridges for cathode and anode side temperature control are placed in the outer stainless-steel plates on each side.

2.3. CCM and PTL

The used CCMs were manufactured at Fraunhofer ISE, Freiburg, Germany, using commercially available materials. The membrane is a Nafion N115 membrane with a thickness of 127 μm. The anode catalyst loading is ~0.5 mg_{Ir}/cm^2, and the cathode catalyst loading is ~0.25 mg_{Pt}/cm^2. The anode catalyst layer consists of iridium(IV)-oxide particles by *ThermoFisher Scientific, Germany* (Premion, 84.5% iridium) and Nafion D2020CS ionomer with an ionomer to solid ratio of 16.68 wt%. The cathode catalyst layer consists of platinum black catalyst particles by *Umicore AG & Co. KG, Germany* (Elyst Pt50 0550, 50% Pt) and Aquivion D79-25BS ionomer with an ionomer to solid ratio of 29.75 wt %. Both catalyst layers were produced by slot-die coating on a decal foil and hot pressed onto the membrane. As PTL commercially available titanium materials from *NV Bekaert SA* (type 2GDL06-0.25) with a thickness of 250 μm are used at both anode and cathode. To compensate for the height of the PTL, PTFE gaskets with the same thickness are used in the outer area.

2.4. Measurement equipment and methods

To measure polarization curves and impedance spectra, a Zahner Zennium X combined with a Zahner PP241 power potentiostat was integrated into the test bench. These devices from *Zahner-Elektrik GmbH & Co. KG, Germany* enable dc and ac currents up to 40 A at cell voltages up to 4 V. Regarding impedance spectroscopy, a frequency range from 10 μHz to 12 MHz is feasible.

The polarization curves are performed with holding times of 2 min for each current density step, ranging from 1 mA cm^{-2} to 7 A cm^{-2} with varying step size. In total, 34 points are measured along the curve. For the data acquisition, only the last 10 s of the 2 min holding time are considered to ensure a stable cell voltage.

The EIS measurements are performed in galvanostatic mode at different dc bias currents, ranging from 1 mA cm^{-2} to 7 A cm^{-2}. Before each measurement of an impedance spectrum the cell was operated at the selected conditions for 15 min. For the impedance measurement an ac signal with a small perturbation of 10% of the dc bias is applied. The impedance spectra are measured in a frequency range from 100 kHz to 100 mHz with a frequency resolution of 10 steps per decade and an integration time of 10 periods. For further information on the EIS method, we refer to Refs. [26–28].

To ensure the data quality of the measured impedance spectra for the following analysis, the Kramers-Kronig transformation of the impedance data [29] is applied. This method uses the link between the real and imaginary parts of the impedance spectrum (Equations (1) and (2)) to verify that the requirements of causality, linearity, and time-invariance are met.

$$Z_{Re}(\omega) = \frac{2}{\pi}\int_0^\infty \frac{\omega' \cdot Z_{Im}(\omega')}{\omega^2 - \omega'^2} d\omega' \tag{1}$$

$$Z_{Im}(\omega) = -\frac{2}{\pi}\int_0^\infty \frac{\omega \cdot Z_{Re}(\omega')}{\omega^2 - \omega'^2} d\omega' \tag{2}$$

$Z_{Re}(\omega)$ represents the real part of the impedance, $Z_{Im}(\omega)$ the imaginary part and ω the angular frequency. Since there is no analytical solution to this semi-infinite integral, a Kramers-Kronig compliant model consisting of a series connection of RC-elements is fitted to the measured data using the method outlined in Ref. [29]. The conformity of the measured spectrum with the fitted model can be judged by the residual:

$$\Delta_{Re}(\omega) = \frac{Z_{Re}(\omega) - \widehat{Z}_{Re}(\omega)}{|Z(\omega)|} \tag{3}$$

$$\Delta_{Im}(\omega) = \frac{Z_{Im}(\omega) - \widehat{Z}_{Im}(\omega)}{|Z(\omega)|} \tag{4}$$

With $|Z(\omega)|$ representing the absolute value of the measured impedance and $\widehat{Z}(\omega)$ the model impedance. Exemplary data for the Kramers-Kronig test results are shown for a variation of current density in Figure SI1 (Supplementary Information). The invalid data, especially at the high frequency end, which is related to inductive coupling between ac current supply and voltage measurement as well as further electrical noise in the lab, is excluded from the results. As a criterion for accepting data quality, a deviation of 2% is used, with most data remaining well below 1%.

To analyze the impedance data in more detail, the DRT is used for the identification and deconvolution of different polarization processes differing in their characteristic time constants. For detailed information on the method, we refer to Refs. [30,31]. Equation (5) shows the link between an impedance $Z(\omega)$ and its distribution function $g(\tau)$ of relaxation times τ [31]:

$$Z(\omega) = R_0 + \int_0^\infty \frac{g(\tau)}{1 + j\omega\tau} d\tau \tag{5}$$

R_0 is the ohmic resistance of the spectrum. For the DRT-calculation of the measured spectra, we employ a numerical approach, which is based on a fit to the real part of the impedance spectrum. For stabilization the Tikhonov regularization [31,32] is used. A regularization parameter λ of 0.005 was found to be the optimal value for the measurements in this study, as shown in Figure SI2 (Supplementary Information) for an exemplary λ variation. Too low values of λ show randomly appearing peaks that cannot be attributed to physico-chemical processes, while too high values cause problems with resolving individual peaks and result in decreased data quality in the Kramers-Kronig test.

Typically, the DRT only displays the capacitive processes. To incorporate the negative inductive processes at low frequencies, we used an adapted DRT calculation that allows for negative resistance and capacity values in specific parts of the spectrum, as introduced by Schiefer et al. [33].

2.5. Measurement procedure

As a conditioning procedure, a standard method previously developed for the CCM from Fraunhofer ISE is employed. This procedure consists of a swelling period with water flow at the anode side for 90 min, during which the temperature is increased to the desired value of 80 °C within the first 30 min and then maintained constant for an additional 60 min. Afterwards, voltage steps are performed from 1.5 V to 2.0 V in 0.1 V steps, holding each voltage for 10 min. Next, four polarization curves are measured, ranging from low to high currents and back again to low currents, starting at 0.01 A cm^{-2} and increasing to 7 A cm^{-2} or until the voltage limit of 3 V is reached. Each of the 16 steps is measured for 5 min. These polarization curves take a total of 640 min. Afterwards, a voltage of 1.9 V is applied for 5 h, and then a voltage of 2.1 V for 10 h. After this conditioning procedure of approximately 28 h, the CCM is expected to exhibit stable performance, allowing for comparable measurements to be performed.

For each type of CCM/PTL combination, it is meaningful to conduct a compression test to determine the optimal compression force for the active area. For this, we manually increased the compression of the active area by the middle screw of our incremental test cell after conditioning at 1 MPa. We then performed one EIS measurement for each compression. The applied compression is calculated by dividing the force measured by our force sensor by the contacted area of our stamp. Considering the flow field design used in this study, only the land area of 1.2 cm^2 is considered.

As the reference point (RP), testing at a temperature of 60 °C, ambient pressure, and a water flow rate at the anode of 10 mL min^{-1} cm^{-2} (which equals a total flow of 21 mL min^{-1} for the incremental test cell) are chosen. Under these conditions, a polarization curve and an EIS measurement at 2 A cm^{-2} are performed. The measurements at the reference point are repeated after each measurement series to determine if the cell performance has been affected by the varied operating conditions or measurements performed in between.

The reproducibility and stability of our setup and cell were evaluated by testing different nominally identical samples as well as comparing the results for one sample after each measurement series conducted.

In the main part of this study, different parameter variations are performed to evaluate operating parameter dependencies of the DRT-peaks, which is the basis to determine the physicochemical background of the underlying electrochemical processes. Only one parameter is varied during one parameter variation, while the rest are kept at the standard operating point. A cathode overpressure variation between 0 bar and 10 bar, a temperature variation between 30 °C and 80 °C, and a water flow rate variation at the anode between 5 mL min^{-1} cm^{-2} and 30 mL min^{-1} cm^{-2} were performed. The cathode is operated without any external water or gas supply during all measurements; only the generated hydrogen and the diffusing/drag water are fed to the cathode compartment. The procedure results in 16 operating points, at each of which one polarization curve and 10 EIS measurements at different dc currents are performed, resulting in an overall testing time of approximately 185 h per cell.

3. Results

3.1. Compression force variation

The compression test results for a variation of compression between 1 MPa and 7 MPa are shown in Fig. 3 a) and b) in the Nyquist and DRT plot, respectively, for a current density of 2 A cm^{-2}. The total polarization resistance is hardly affected by changes in compression and varies only between 21.6 mΩ cm^2 and 24.3 mΩ cm^2. Minor variations are observed in the high-frequency peak P_4 in the DRT, which is connected to HER and/or proton conduction in the ionomer of the anode, based on the findings shown in Table 1, but no clear trend is discernible. P_3 in the medium frequency region, connected to charge transfer kinetics, remains stable with the compression force variation. In the low-frequency region, the two peaks P_1 and P_2, which are related to mass transport losses (see Table 1), are strongly overlapping at certain compressions, making it difficult to identify a definite trend. Conversely, the observed ohmic resistance clearly depends on the compression force, decreasing by 4.7 mΩ cm^2 as compression increases up to 5 MPa, after which no further improvement is seen at 7 MPa. Therefore, the applied compression of 5 MPa is considered to be sufficient for an appropriate contacting of the evaluated CCM-PTL combination and is thus used in the further tests.

3.2. Reproducibility and stability

Before conducting a detailed parameter variation, we first wanted to verify the stability and reproducibility of our measurement setup. Therefore, 7 nominally identical CCM samples, as introduced in Section 2.3, were tested. The reproducibility is evaluated using the results obtained during the first reference point measurements after conditioning. The results are shown in Fig. 4, including the polarization curve in Fig. 4 a), the Nyquist plot in 4 b), the DRT plot in 4 c), and a resistance and voltage plot in Fig. 4d). Analyzing the polarization curve in Fig. 4 a), it is evident that all tested samples perform almost identically up to about 2 A cm^{-2}. From this point forward, differences between the samples become noticeable in the polarization curves. One aspect of the differences arises from changes in the ohmic resistance, as shown in the Nyquist presentation in Fig. 4 b), as well as in the resistance plot in Fig. 4 d). The ohmic resistance ranges between roughly 120 mΩ cm^2 and 136

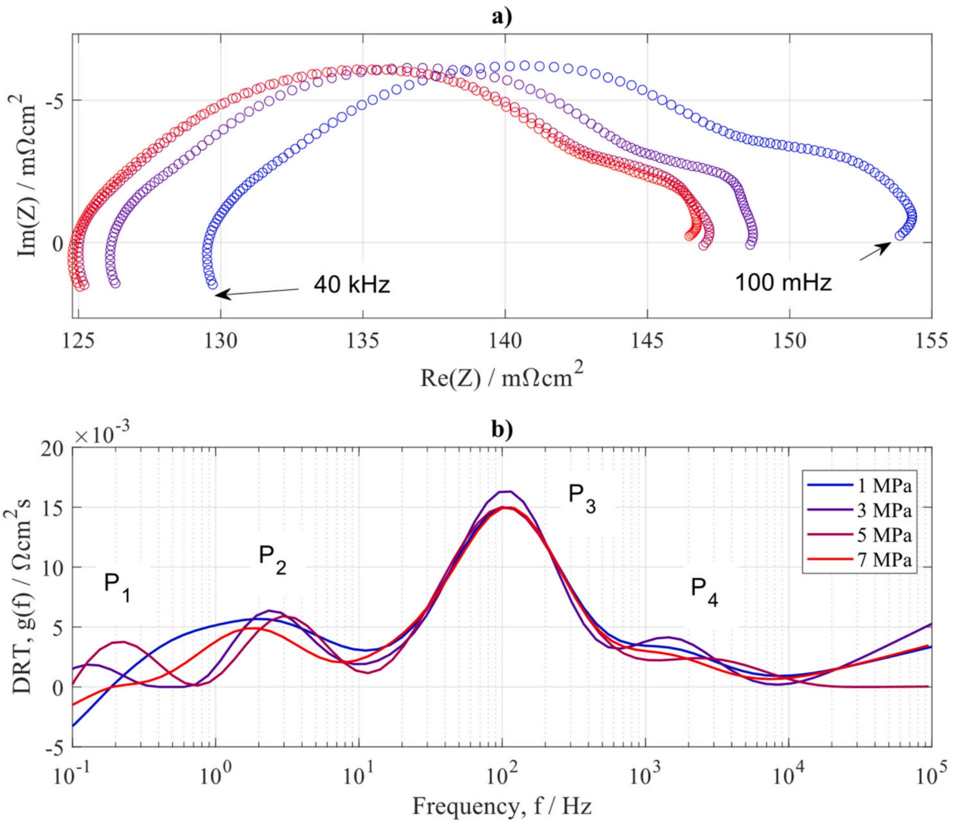

Fig. 3. a) Nyquist plot and b) DRT plot of a compression force variation between 1 and 7 MPa at 2 A cm^{-2}.

Table 1
Frequency ranges, parameter dependencies, and possible physical origin of identified polarization processes.

Process	Characteristic frequency	Dependencies	Possible physical origin
P_{ind}	<1 Hz	i ↑, T ↓, p ↑	Membrane humidification effect [12], changing iridium states [12], and/or transient thermal effect [40]
P_1	0.1 - 30 Hz	i ↑, T ↓, p ↑	Mass transport
P_2	3 - 200 Hz	i ↑, T ↓, p ↑	Mass transport
P_3	1 -10^3 Hz	i ↓, T ↓, p ↓	Charge transfer kinetics (OER or combined OER & HER)
P_4	10^2 - 10^4 Hz	i ↓	Charge transfer kinetics at the cathode (HER) and/or proton conduction in the ionomer of the anode
P_5	10^3 - 10^5 Hz	i ↓, T ↓	Proton conduction in the ionomer of the anode

mΩ cm^2. Further differences between the samples appear in the low-frequency region of the spectrum, which is related to mass transport losses, as shown in Fig. 4 c) in the DRT presentation for frequencies between 10^{-1} and 10^1 Hz. This is also visible from the total polarization resistance plotted in Fig. 4 d). The total cell voltage is also displayed in Fig. 4 d), showing the same trends observed earlier. The differences seen can be attributed to the following factors: The materials are not commercially produced, so small variations among different CCM samples have to be expected. Our test cell is designed and manufactured in-house, and it must be assembled carefully to ensure proper compression on the active area. Additionally, the CCMs are laminated to the required size manually, and the entire assembly is done by hand with many small parts that need to be placed correctly. Here, we can also observe that the first tests show greater variations (see Test 1 to 3). With a better routine in the cell mounting procedure, these variations significantly decrease, and a slight trend toward improved performance is noticeable in the last four samples. Despite of this, deviations < ± 25 mV at 2 A cm^{-2} could not be prevented.

To be able to analyze the data obtained within the different operating parameter variations and extract parameters for reliable cell performance modeling, it is essential that the health state of the cell does not change during these tests. To analyze this, we compare the data obtained during the reference point measurements of Test 7, presented in Fig. 4 e)-h), with e) displaying the polarization curves, f) the Nyquist plots, g) the DRT plots, and h) the resistance and voltage plot of the corresponding RPs. For the cell shown here, the RP measurements were repeated 6 times during 155 h of testing. The data shows that performance remains within a similar range across all RPs over the entire current density region, as depicted in the polarization curves in Fig. 4 e). Slight variations occur in the ohmic resistance, visible in the Nyquist plot in Fig. 4 f) and the resistance plot in Fig. 4 h), with a reduction for RP3 and RP4 before resistance increases again for the last two RPs. The polarization resistance in Fig. 4 h) and the peaks in the DRT in Fig. 4 g) exhibits no notable differences. This indicates that our setup, cell, and CCM operate stable throughout the entire testing procedure, and their health state is not affected by the parameter variations.

After ensuring a reproducible and stable operation of the cell, the results of the different operating parameter variations will be discussed in the following sections using data collected from Test 7. Impedance spectra and related DRTs will be discussed, considering the peaks in the DRT and how they are influenced by the varied operating parameters.

3.3. *Current density variation*

The current density was varied from 0.01 A cm^{-2} to 7 A cm^{-2}. Measurements at OCV were avoided as this is a rather undefined state for PEM fuel cells and electrolyzers resulting in not meaningful

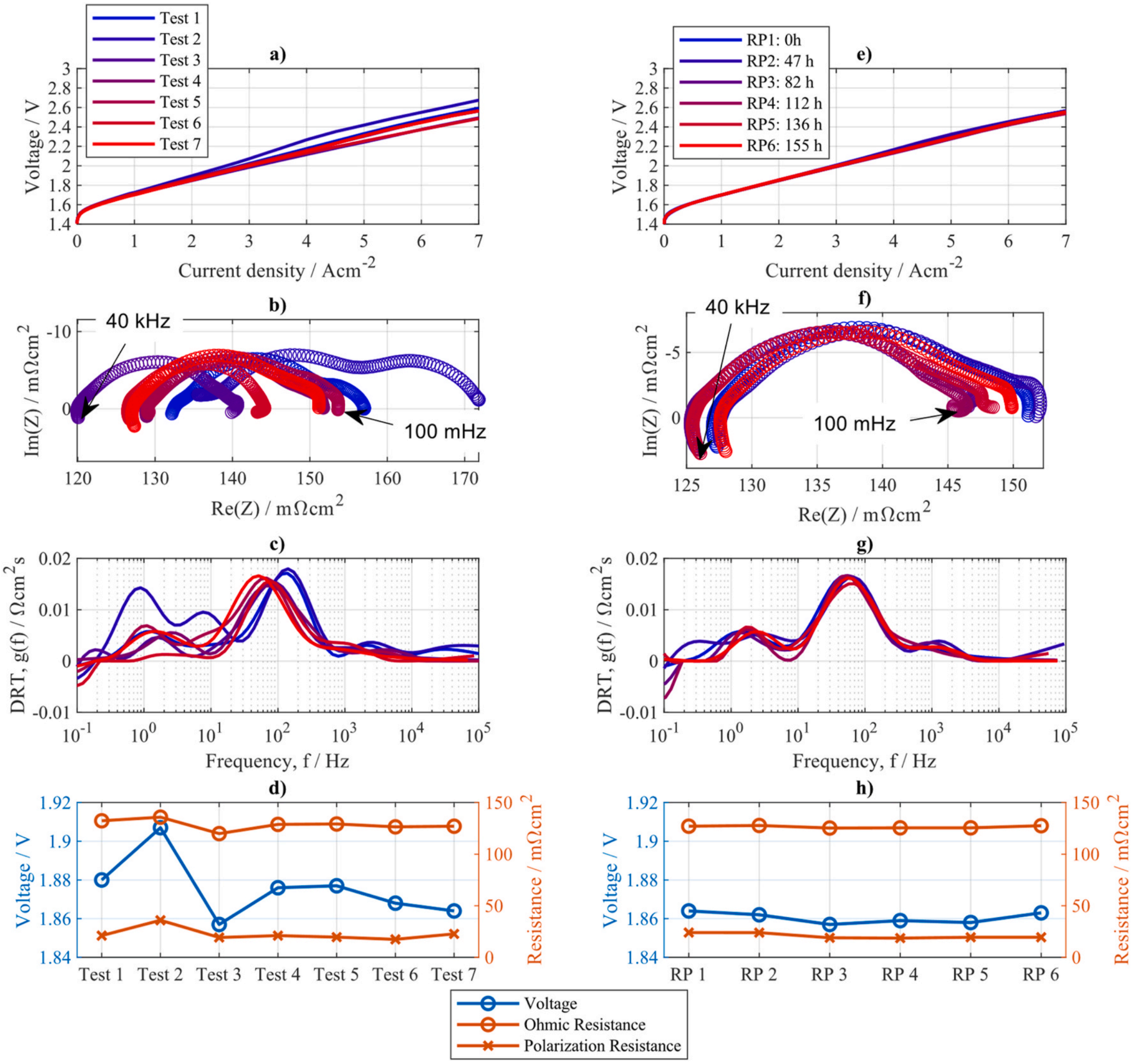

Fig. 4. a), e) Polarization curves, b), f) Nyquist plots, c), g) DRT plots, and d), h) voltage and resistance plots at the reference point of 7 different cells to check reproducibility of cell and test setup (a, b, c, d) and of one cell during a test of 155 h with various operating parameter variations (e, f, g, h).

polarization values. In Fig. 5, the variation is divided into four current density regions for better visibility of the effects in each region. On the left side of the figure (Fig. 5 a), c), e), and g)), the Nyquist plot is displayed, while on the right side (Fig. 5 b), d), f), and h)), the corresponding DRT presentation is shown. In Fig. 5a) and b), current densities between 0.01 A cm^{-2} and 0.25 A cm^{-2}, with a step size of 0.05 A cm^{-2} (0.04 A cm^{-2} for the first step), are shown. In this region, we observe only one deformed semicircle in the Nyquist plot, which decreases significantly with increasing current density, especially during the first 3 steps. The ohmic resistance remains stable across all measurements. In the DRT presentation, we observe a major peak labeled as P_3 in the figure, starting at a frequency of 0.3 Hz with 0.01 A cm^{-2}, which then decreases and shifts toward higher frequencies. At 0.25 A cm^{-2}, the peak is already located at 7 Hz. A second peak labeled P_4, partly overlapping with peak P_3, also decreases with increasing current density. This behavior might be explained in two different ways: These peaks could represent (i) the kinetics of the anode and cathode respectively, with P_3 representing the larger polarization resistance of the anode at lower relaxation frequencies or (ii) P_3 representing the charge transfer polarization of the anode whereas P_4 is attributed to the proton conduction in the ionomer. Such DRT-behavior, one main peak at the lowest frequency, representing charge transfer kinetics, and additional peaks at higher frequencies, decreasing in size with increasing frequency, has to be considered for various kinds of porous electrodes and can be described by a transmission line model approach [34]. Anyhow, next to one of these options it can also be a combination of (i) and (ii) as for example shown for SOCs in Ref. [1] and PEM fuel cells in Ref. [2].

Examining the next current density region shown in Fig. 5 c) and d), which displays current densities from 0.25 A cm^{-2} to 1.5 A cm^{-2} in 0.25 A cm^{-2} increments, we observe that the same trend continues. In the Nyquist plot, we observe one main semicircle that is further decreasing. Additionally, at the higher current densities, a small second semicircle appears in the low-frequency region. The ohmic resistance remains constant within this current density range. Examining the DRT presentation, we still observe the major peak P_3 decreasing and shifting to higher frequencies. Additionally, we notice the further decreasing peak P_4 at higher frequencies, and additional peak(s) $P_{1,2}$ emerging in the low-frequency region around 0.8 Hz. The continued decrease of P_3 and P_4 supports our assumption that these are charge transfer and/or proton conduction processes.

In Fig. 5 e) and f), the results for current densities ranging from 1.5 A cm^{-2} to 4 A cm^{-2}, with a step size of 0.5 A cm^{-2}, are shown. In this region, we observe a change in trend when examining the Nyquist plot. Up to 2 A cm^{-2}, the polarization resistance continues to decrease. Starting at 2.5 A cm^{-2}, the trend reverses, and an increase in the overall polarization resistance becomes apparent. This suggests that there are

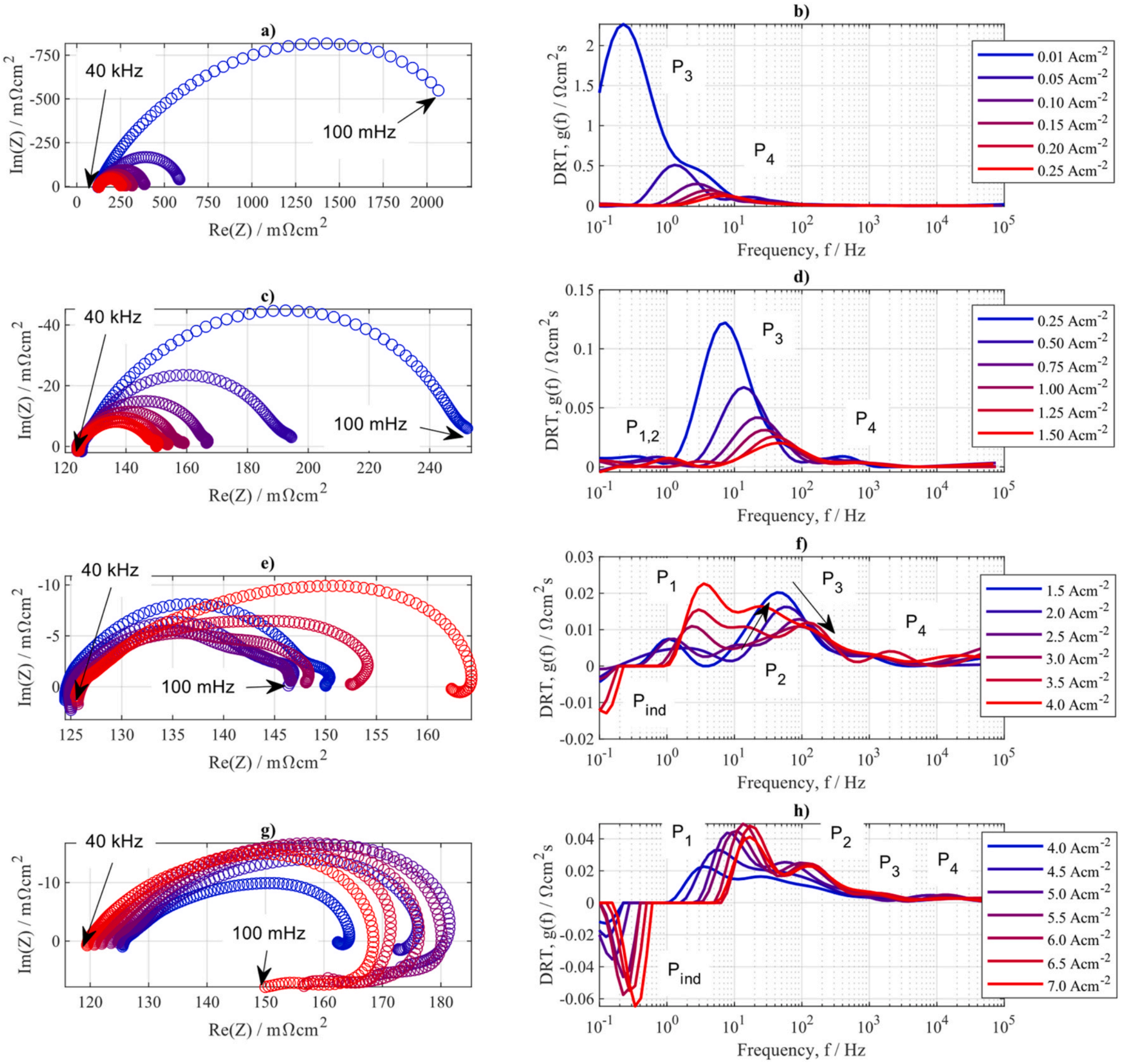

Fig. 5. a), c), e) and g) EIS and b), d), f), h) DRT presentation of a current density variation between 0.01 Acm^{-2} to 7 Acm^{-2} split into different current density regions at the reference point (60 °C, 0 bar, 10 ml$_{H2O}$min^{-1}cm^{-2}).

additional processes with a contrary current density dependency to P_3 and P_4 that were not detectable in the lower current density regime. Furthermore, in the Nyquist plot for 4 A cm^{-2}, an inductive loop begins to form at low frequencies, which is consistent with our previous investigations [11,12]. In the DRT plot, we can still observe the peak P_3, which decreases until 2.5 A cm^{-2}. After that, it appears to stabilize, but it also overlaps with the rising peak from the lower frequency region, making the overall trend difficult to interpret. In the lower frequency region, we now observe the formation of up to two new peaks, labeled P_1 and P_2 in the figure, which increase with current density. This behavior indicates that these processes might be linked to mass transport limitations by diffusion, which commonly increase with the current density. Additionally, we observe a negative peak, labeled P_{ind}, appearing at the edge of our frequency range at the highest current densities, consistent with the inductive low frequency loop in the Nyquist plot.

This current density region remains largely unexplored in existing research so far. Most studies on process identification using DRT in PEMWE focus on low current densities. Two publications by Zou et al. [9,10] explore loss mechanisms in PEMWE that consider current densities up to 2 A cm^{-2}. They did not observe this change in trend, but the results are still in agreement as current densities of 2.5 A cm^{-2} and more were not investigated. In Ref. [35] we investigated the use of carbon-based porous transport layers at the cathode in combination with ultra-low cathode catalyst layer loading for current densities of up to 3 A cm^{-2} and also saw increasing processes in the low-frequency region, that was attributed to cathode mass transport.

Results at even higher current densities of 4 A cm^{-2} to 7 A cm^{-2} with a step size of 0.5 A cm^{-2}, are shown in Fig. 5 g) and h). There is a lack of comparable literature data examining the loss processes in this current density range in detail. We observe an increase in the total polarization resistance until 5 A cm^{-2} in the Nyquist plot in Fig. 5 g). Furthermore, we observe a decrease in ohmic resistance with increasing current density that started already at 3.5 A cm^{-2}. This change is likely due to a temperature change related to self-heating in the CCM at higher current densities, leading to a lower ohmic resistance. The decrease in ohmic resistance agrees with the performed temperature variation (Fig. 7). Assuming that the ohmic resistance decrease is determined by the temperature dependency of the membrane conductivity, the self-heating creates a rise of the membrane temperature of below 5 K for the measurement at 60 °C and 7 A cm^{-2} (see Section 3.5 for details). The capacitive polarization resistance stagnates above 5 A cm^{-2}, as shown in the DRT plot in Fig. 5 h). The inductive loop and corresponding peak in the DRT, on the other hand, continue to grow, which could be overshadowing the increase in the capacitive area. The negative peak is increasing across the entire current density range measured and is also shifting to higher frequencies. This inductive peak has been frequently observed in recent PEMWE studies and becomes more prominent as current density increases and voltage rises. Its origin has not yet been fully understood. What is clear is that it is challenging to separate the low-frequency capacitive processes from the inductive loop, as the latter may overshadow the former.

For the capacitive processes visible in the DRT in this current density region, we can now hardly see peaks P_3 and P_4 anymore. Instead, we only observe the two increasing peaks in the lower frequency region, P_1 and P_2, which we already started to see in the previous current density region. They continue to increase until around 5 A cm^{-2} and shift to higher frequencies. This simultaneous increase in polarization resistance and relaxation frequency must be related to a decreasing (pseudo-) capacity of the related process. Above 5 A cm^{-2}, P_1 and P_2 begin to stabilize. It is essential to note that at high current densities, voltage fluctuations are more pronounced than at lower current densities, likely due to the strong formation of gas bubbles. This is also reflected in the impedance data quality, where higher current densities lead to increased fluctuations in the Kramers-Kronig test. Since these fluctuations remain below 1%, the data is still considered valid. Due to the significant changes caused by different current densities, in the further investigations of parameter variations, we selected three distinct current densities to examine the results across the entire current density range. These are 0.1 A cm^{-2}, 2 A cm^{-2} and 5 A cm^{-2}. Analyzing such data at significantly differing current densities, it has to be considered that the common approach to attribute an electrochemical process in a cell to a more or less fixed relaxation frequency is incorrect and will result in severe misinterpretation of impedance data. The stepwise increase in current density with rather small current density steps reveals that the relaxation frequency of a peak can vary significantly for P_3 for example from the 100 mHz to 1 kHz and additional peaks related to different physicochemical phenomena might appear in a frequency range previously occupied by a different process. This can also be explained by the relaxation frequency f, which is given by the following equation:

$$f = \frac{1}{2 \cdot \pi \cdot \tau} = \frac{1}{2 \cdot \pi \cdot R \cdot C} \tag{6}$$

with τ the relaxation time, calculated from the product of the resistance R and the capacitance C. The resistance of P_3, which relates to charge transfer kinetics based on the findings shown in Table 1, decreases exponentially with increasing current density as described by the Butler-Volmer kinetics. As this resistance decreases and if the capacitance remains constant, the relaxation time shortens, leading to an increased frequency.

3.4. Cathode pressure

We performed a differential pressure variation test from 0 bar to 10 bar at the cathode, as shown in Fig. 6, across three current density regions: a) and b) at 0.1 A cm^{-2}, c) and d) at 2 A cm^{-2}, and e) and f) at 5 A cm^{-2}. Due to stability issues with the applied CCM-PTL combination, higher differential pressures had to be avoided.

Examining the ohmic resistance in the Nyquist plots, there's an observable increase, especially at 2 A cm^{-2} for higher pressures (5 bar and 10 bar). This could be due to poorer contact between the flow field

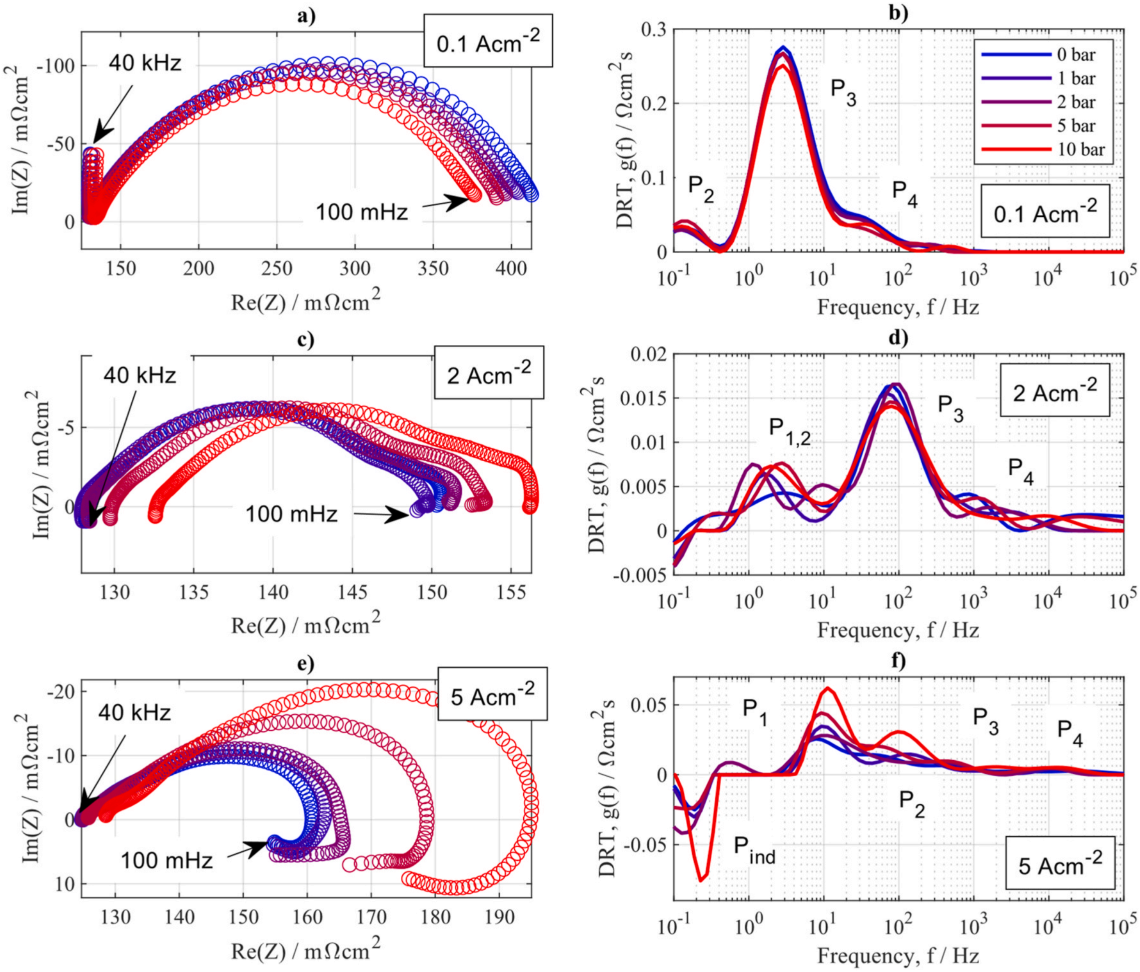

Fig. 6. a), c), and e) Nyquist plot, and b), d), and f) DRT plot of a pressure variation at the cathode side between 0 bar and 10 bar. Current densities of 0.1 Acm^{-2} in a) and b), 2 Acm^{-2} in c) and d), and 5 Acm^{-2} in e) and f).

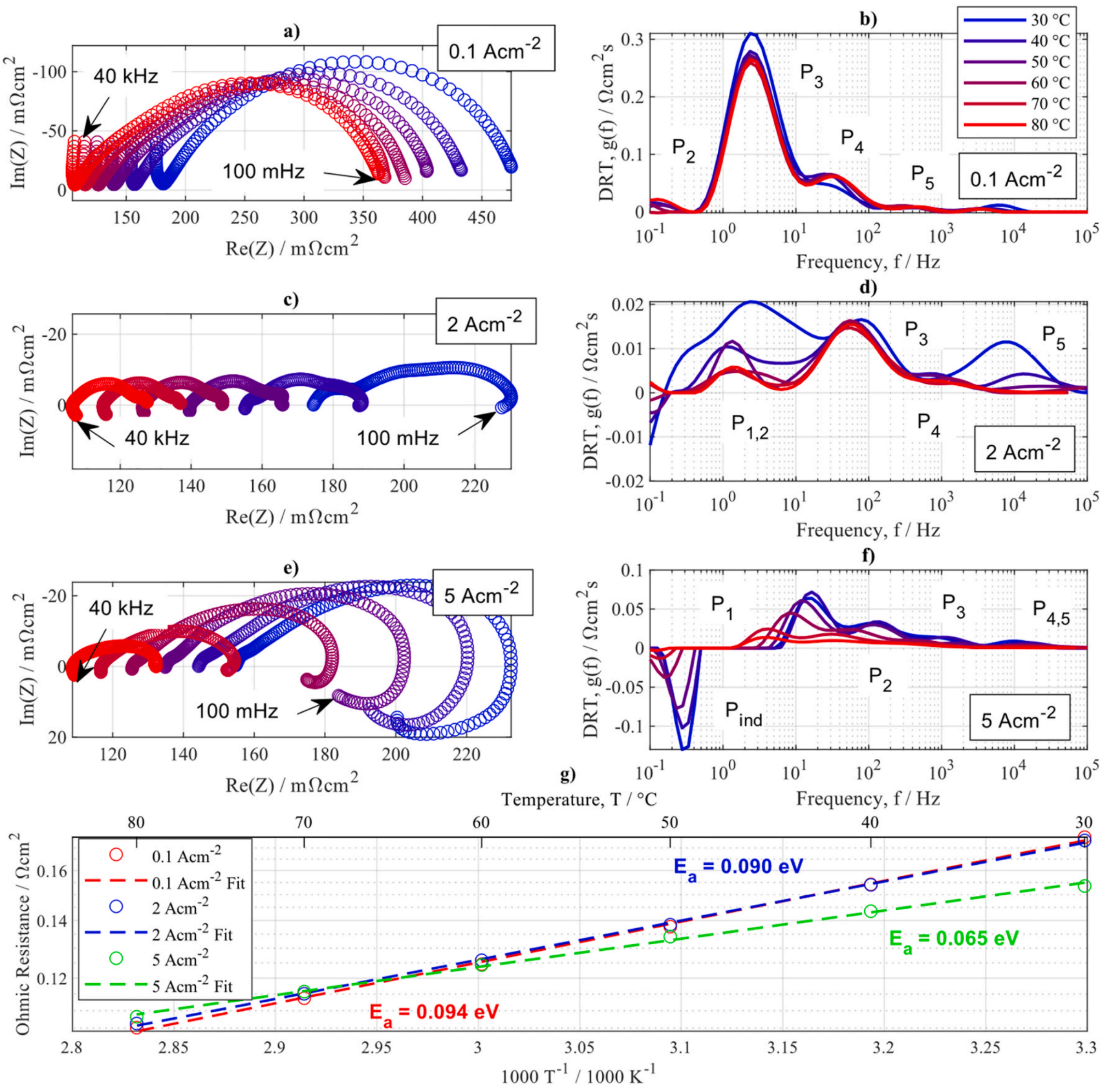

Fig. 7. a), c), and e) Nyquist plot, b), d), and f) DRT plot, and g) Arrhenius plot of a temperature variation between 30 and 80 °C. Current densities of 0.1 A cm^{-2} in a) and b), 2 A cm^{-2} in c) and d), and 5 A cm^{-2} in e) and f).

and PTL. The differential pressure, applied to the cathode side, which is located on the bottom side of the cell, might cause the PTL to bend slightly, reducing its contact area with the flow field. The polarization resistance at different current densities shows strong differences in behavior. For the low current density (0.1 A cm^{-2}), as shown in Fig. 6 a) and b), a small improvement in the total polarization resistance is observed. In the DRT, this appears to be associated with a decrease in P_3 and P_4. This aligns well with the results presented in Refs. [9,10], where they observe an enhancement of the kinetics of the charge transfer processes with pressure. At the high-frequency region in the Nyquist plot, we observe that the curve rises again into the capacitive region, instead of descending into the inductive region as seen for the other current densities. This may suggest that another high-frequency process is starting here, which we are unable to access with our setup.

In the medium current density region (2 A cm^{-2}), shown in Fig. 6 c) and d), the total polarization resistance appears to be stable, as seen in the Nyquist plot. In the DRT plot, there are minor deviations in the different peaks, but no clear trends are visible.

In the high current density region (5 A cm^{-2}), shown in Fig. 6 e) and f), the behavior changes drastically. The polarization resistance now increases significantly with pressure, and an inductive loop that also grows with pressure can be seen in the Nyquist plot. In the DRT plot, we observe an increase in peaks P_1 and P_2, as well as the inductive peak P_{ind}. Peaks P_1 and P_2 are likely associated with different mass transport losses. Therefore, we can conclude that, in our setup, higher pressure greatly amplifies the mass transport limitations. This effect is partially obscured by the simultaneous increase of the inductive process. As a result, the actual increase in mass transport losses could be even more substantial than what is apparent here. For the inductive process, Zuo et al. [10] observe a similar trend with increasing pressure. As an explanation, they say that it might be linked to interfacial effects. In our previous investigations [12] on the inductive loop, we did not observe a pressure impact, but we had only investigated pressures up to 4 bar at that time. Also, we used another CCM type with much higher loading compared to the one used in this study.

For the mass transport processes, some studies [36,37] did not observe an increase with pressure at high current densities, but rather an improvement. In contrast, others observed similar behavior at high current densities as we did [38]. Generally, the behavior under pressure is still not well understood. Garcia-Navarro et al. [24] provided an overview of studies showing that no clear conclusion can yet be drawn regarding whether pressure has a positive or negative impact on current density. In general, higher pressure is expected to reduce gas bubble size, which should help with bubble removal. However, in our tests, as in many others, the anode side is kept at ambient pressure; therefore, only the cathode side can be affected by this change in bubble size. This one-sided compression can lead to deformation of the inner parts, such as bending the PTL and/or CCM, which in turn can change contact and possibly the mass transport regime on both sides. Additionally, the overpressure on the cathode side increases H_2 crossover to the anode, possibly leading to higher mass transport losses due to the counter flow of protons and H_2.

Comparing results of different studies is challenging due to varying test cell setups, materials, and the lack of a standard testing procedure. These factors can significantly impact the behavior.

3.5. *Temperature*

A temperature variation in the range of 30 °C to 80 °C is shown in Fig. 7 for the three different current densities of a), b) 0.1 A cm^{-2}, c), d) 2 A cm^{-2} and e), f) 5 A cm^{-2}. At all current densities, the ohmic resistance decreases as the temperature increases, which is visible in the corresponding Arrhenius plot shown in Fig. 7 g). This behavior is due to the improved conductivity of the membrane. A decrease of 1.4 mΩ per °C in ohmic resistance can be observed at a current density of 0.1 A cm^{-2} by comparing the ohmic resistances of the 30 °C and 80 °C measurement. At 2 A cm^{-2}, the pattern is similar, only a minor temperature increase of 1.5 °C occurs based on the comparison to the 0.1 A cm^{-2} results. For the very high current densities (exemplarily shown for 5 A cm^{-2}) the slope in the Arrhenius plot noticeably flattens. This phenomenon is attributed to a self-heating effect, increasing towards higher current densities and lower temperatures. A temperature increase of 17.1 °C is observed for the measurement conducted at 30 °C and a current density of 5 A cm^{-2}. An overview of the self-heating effect is provided in Table SI1 (Supplementary Information). Figure SI3 illustrates the power loss density P_{loss} (a)), the measured temperature deviation (b)), and the ohmic resistance (c)) as functions of current density for all measured operating temperatures. At lower operating temperatures, the power loss exhibits higher values due to increased resistance, thereby generating more heat. Consequently, the temperature increase at higher current densities diminishes with rising operating temperature until no temperature increase is detectable anymore at 80 °C.

Additionally, it is necessary to consider the heat dissipation to the environment. Given that the cell is metallic and uninsulated, heat dissipation amplifies with increasing operating temperature. As a result, the ohmic resistance ceases to decrease with increasing current density at elevated temperatures. Specifically, at 80 °C, a slight increase in ohmic resistance with respect to current density is observed. This might be attributed to a counteracting effect, namely, that at higher temperatures, the produced gases can absorb a higher amount of water, resulting in an enhanced drying of the membrane.

For the polarization processes at low current densities (0.1 A cm^{-2}) shown in Fig. 7 a) and b), a slight decrease with increasing temperature is observed for peak P_3. This behavior is expected, as electrode kinetics are generally faster at higher temperatures. For 2 A cm^{-2}, on the other hand, we see much stronger changes. P_3 and P_4 now remain constant, but we observe a further peak (P_5) forming at high frequencies at low temperatures. This peak was not visible in previous results because it only becomes apparent at temperatures below 60 °C, which were not investigated before. In different studies [8–10], this peak at high frequencies has been associated with proton conduction in the ionomer of the catalyst layer, showing the same trend of decreasing with increasing temperature. In the low-frequency region, there are up to two peaks, P_1 and P_2, which decrease as the temperature increases. This behavior is supported by Suermann et al. [37], who observe the same trend in their measurements.

In Fig. 7 e) and f), the results for 5 A cm^{-2} are shown. Here we observe the same trend for the peaks P_1 and P_2 as in the medium current density region. Additionally, we see the inductive peak P_{ind} forming and increasing as the temperature decreases, indicating that the inductive behavior is a temperature-activated effect.

3.6. *Water flow rate*

Another parameter variation we examined is the water flow rate at the anode side. We changed the flow rate between 5 mL min^{-1} cm^{-2} and 30 mL min^{-1} cm^{-2}, which corresponds to a total flow rate between 10.5 mL min^{-1} and 63 mL min^{-1} for our incremental test cell, respectively. This is shown in Fig. 8 for the three different current density regions (a), b) 0.1 A cm^{-2}, c), d) 2 A cm^{-2}, and e),f) 5 A cm^{-2}). In general, there is always a significant water excess (stoichiometry $\lambda > 100$), and no water depletion, as observed in Ref. [39] at λ values below 5, is expected, since only about 0.3 mL min^{-1} is used for the reaction and the water drag together at the highest current density of 7 A cm^{-2}, assuming a drag coefficient of 3. The lowest water-to-gas volume ratio in the anode compartment is still above 10%.

Compared to the other parameter dependencies discussed earlier, no strong dependency of the loss processes on the water flow rate is observed. For the low current density shown in Fig. 8 a) and b), no changes with the flow rate are visible at all. In Fig. 8 c) and e), for medium and high current densities, a slight decrease in ohmic resistance with decreasing flow rate is observed. This is most probably caused by an increase in temperature at the lower water flow rate. With less water available, the temperature at the active area rises due to reduced cooling, leading to a decrease in ohmic resistance. In the DRT plot for medium current densities in Fig. 8 d), there is no clear trend for any peak. For the high current density region shown in Fig. 8 f), we observe a change in P_1 at the lowest water flow rate. This might be attributed to a more significant temperature rise at 5 mL min^{-1}, as also visible from the change in ohmic resistance.

It can be concluded that the flow rate in the investigated range does not significantly affect performance; a temperature increase is most likely the cause of the observed effects. Lower flow rates were not tested because they no longer exhibited stable temperature behavior, and the requirement of zero gradients for the incremental cell will no longer be fulfilled.

4. Discussion

With the parameter variations conducted, we can offer initial insights into the possible physical origins of the different peaks in the DRT. In Table 1, we provide an overview of the peaks, their characteristic frequencies, how they depend on the parameter variations performed, and ideas for their potential physical origins. Here, i represents the current density, T the temperature, and p the pressure. The arrows next to the different dependencies indicate whether the corresponding peak is rising or falling as the associated parameter increases.

For the inductive peak P_{ind}, which occurs in the low-frequency region below 1 Hz, we observed a dependency on current density, temperature, and pressure in this study. In our previous investigations [12], we suggested relations to membrane humidification effect and changes in iridium oxidation states. A recent publication by Franz et al. [40], however, modeling our measurement data, concluded that it is a transient thermal effect. P_1 and P_2 are considered to be mass transport-related processes because they occur in the lower frequency region (0.1 Hz to 200 Hz) and increase with higher current density. If these two processes are linked to cathode and anode side or to different functional layers as PTL and electrode needs to be explored in future studies. Li et al. [4] also observed two peaks for the mass transport but provided no further explanation. P_3 is the dominant process at low current densities and decreases significantly as the current density increases. It is therefore likely related to charge transfer kinetics, either of the anode reaction (oxygen evolution reaction, OER) alone or a combination of the anode and cathode reactions (OER and hydrogen

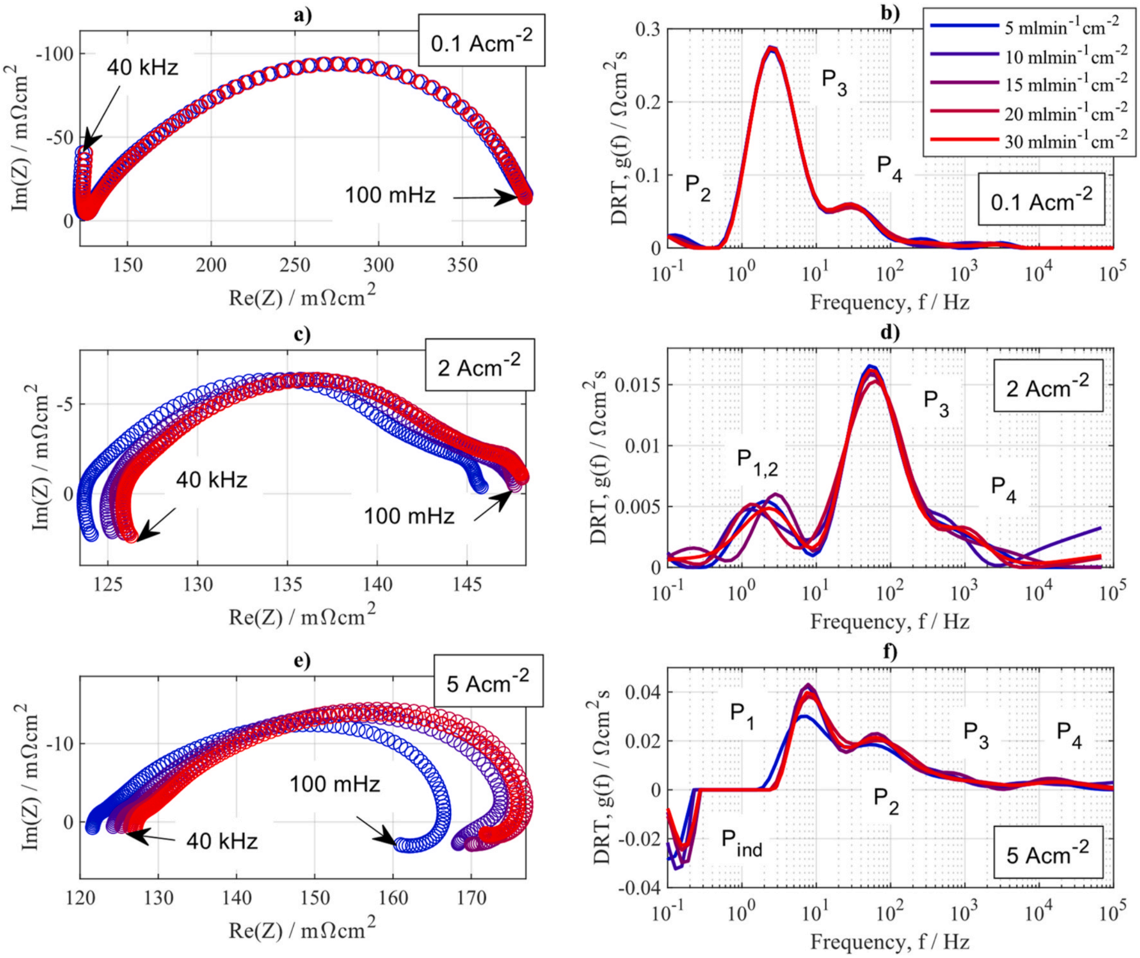

Fig. 8. a), c), and e) Nyquist plot, and b), d), and f) DRT plot of a water flow rate variation at anode side between 5 and 30 ml$_{H2O}$min^{-1}cm^{-2}. Current densities of 0.1 Acm^{-2} in a) and b), 2 Acm^{-2} in c) and d), and 5 Acm^{-2} in e) and f).

evolution reaction, HER). The high-frequency peaks P$_4$ and P$_5$, occurring above 100 Hz, are most probably side peaks of P$_3$ related to the coupling of charge transfer and proton transport in the ionomer [8–10], which can be described by a transmission line model [34], as discussed in Section 3.3. Furthermore, P$_4$ could be strongly affected by the faster charge transfer kinetics of the HER.

From these findings, we can now suggest how to apply this in the practical operation of a PEMWE stack or system. The results indicate the lowest total resistance at a current density of 2 A cm^{-2}. At this current density, the voltage is just below 1.9 V. At this point, mass transport losses are minimal, and activation losses are also low. Therefore, this appears to be an ideal operating point. Additionally, higher temperatures enhance performance and are therefore recommended. However, degradation must be considered, which was not examined here. An optimal balance between degradation and performance needs to be determined.

5. Conclusion

In this study, we performed DRT-based impedance analysis of PEMWE single cells in a newly developed test bench for the pressurized operation of PEMWE single cells. With a zero-gradient test cell exhibiting an active area of only 2.1 cm^2, homogeneous operating conditions were ensured.

Preliminary measurements showed that mounting of the cell can have a significant impact on the obtained performance. We identify 5 MPa as the optimal compression value for our setup. Reproducibility between different samples was compared and we could show that with a more established cell mounting procedure the variations significantly decrease and a good reproducibility could be reached for the last samples. Repeated measurements at a defined reference point were introduced to monitor the health of the cell during different operating parameter variations carried out over a testing period of up to 2 weeks.

Various parameters, including current density, pressure, temperature, and water flow rate, were varied to analyze their impact on the peaks in the DRT. We explored a wide current density range between 0.01 A cm^{-2} and 7 A cm^{-2}, with the high current density region not yet studied in detail in previous works. This variation allowed us to distinguish four capacitive processes and one inductive process, the latter occurring at high current densities only. An additional process was uncovered in the high-frequency region, appearing only at low temperatures. Pressure primarily impacts the high current density region, increasing mass transport processes and the inductive process with increasing pressure. The variation in water flow rate shows only a minor impact, which is reasonable as only lambda values >100 were analyzed.

Our results show that attributing DRT-peaks to electrochemical processes at a fixed relaxation frequency is misleading. Increasing current density gradually revealed that the peaks related to the charge transfer reaction shift their relaxation frequency drastically from the mHz-to the kHz-range. At higher current density additional low frequency peaks that most probably are related to mass transport effects appear, which can be misinterpreted as an increasing charge transfer polarization at increased current densities. Further tests have to be performed for a complete understanding and accurate differentiation between mass transport and charge transfer effects.

CRediT authorship contribution statement

Debora Brinker: Writing – original draft, Visualization, Validation, Software, Methodology, Investigation, Data curation, Conceptualization. **Niklas Hensle:** Writing – review & editing, Resources, Conceptualization. **Gözde Kardeş:** Writing – review & editing, Methodology, Conceptualization. **David Breuninger:** Software, Methodology, Investigation. **Mika Schächinger:** Software, Methodology, Investigation. **August Gladik:** Methodology, Investigation. **Philipp Röse:** Writing – review & editing, Funding acquisition, Conceptualization. **André Weber:** Writing – review & editing, Supervision, Funding acquisition, Conceptualization.

Declaration of generative AI and AI-assisted technologies in the writing process

During the preparation of this work the authors used Grammarly (https://app.grammarly.com) in order to improve the academic tone and accuracy of language, including grammatical structure, punctuation, and vocabulary. After using this tool, the authors reviewed and edited the content as needed and take full responsibility for the content of the publication.

Declaration of competing interest

The authors declare that they have no known competing financial interests or personal relationships that could have appeared to influence the work reported in this paper.

Acknowledgment

The authors gratefully acknowledge funding from the Federal Ministry of Research, Technology and Space, Germany (BMFTR 03HY103C and 03HY103F). We thank Schaeffler Technologies AG & Co. KG, Germany for the collaboration.

Appendix A. Supplementary data

Supplementary data to this article can be found online at https://doi.org/10.1016/j.ijhydene.2026.154048.

Data availability statement

The data presented in the manuscript is openly available in the KITopen repository at https://doi.org/10.35097/hq2hmnh7swww7fvq.

References

[1] Leonide A, Sonn V, Weber A, Ivers-Tiffée E. Evaluation and modeling of the cell resistance in anode-supported solid oxide fuel cells. J Electrochem Soc Jan. 2008; 155(1). https://doi.org/10.1149/1.2801372. Art. no. 1.

[2] Heinzmann M, Weber A, Ivers-Tiffée E. Advanced impedance study of polymer electrolyte membrane single cells by means of distribution of relaxation times. J Power Sources Jan. 2018;402:24–33. https://doi.org/10.1016/j.jpowsour.2018.09.004.

[3] Schichlein H, Müller AC, Voigts M, Krügel A, Ivers-Tiffée E. Deconvolution of electrochemical impedance spectra for the identification of electrode reaction mechanisms in solid oxide fuel cells. J Appl Electrochem Jan. 2002;32(32).

[4] Li Y, et al. Application of distribution of relaxation times method in polymer electrolyte membrane water electrolyzer. Chem Eng J Jan. 2023;451:138327. https://doi.org/10.1016/j.cej.2022.138327.

[5] Tan A, et al. The poisoning effects of Ti-ion from porous transport layers on the membrane electrode assembly of proton exchange membrane water electrolyzers. Chem Eng J Jan. 2023;471:144624. https://doi.org/10.1016/j.cej.2023.144624.

[6] Sánchez Batalla B, Bachmann J, Weidlich C. Investigation of the degradation of proton exchange membrane water electrolysis cells using electrochemical impedance spectroscopy with distribution of relaxation times analysis. Electrochim Acta Jan. 2023:143492. https://doi.org/10.1016/j.electacta.2023.143492.

[7] Sánchez Batalla B, et al. Long-term performance of PEM water electrolysis cells with 3D printed electrodes and low catalyst loading. Int J Hydrogen Energy Mar. 2024;59:480–91. https://doi.org/10.1016/j.ijhydene.2024.01.364.

[8] Chan A-L, Yu H, Reeves KS, Alia SM. Identifying electrochemical processes by distribution of relaxation times in proton exchange membrane electrolyzers. J Power Sources Feb. 2025;628:235850. https://doi.org/10.1016/j.jpowsour.2024.235850.

[9] Zuo J, Steiner NY, Li Z, Hissel D. Quantitative investigation of internal polarization in a proton exchange membrane water electrolyzer stack using distribution of relaxation times. Appl Energy May 2025;386:125543. https://doi.org/10.1016/j.apenergy.2025.125543.

[10] Zuo J, Steiner NY, Li Z, Hissel D. Interpreting full-frequency impedance spectrum for PEM electrolyzers: distribution of relaxation times-based modeling. Appl Energy Sept. 2025;394:126185. https://doi.org/10.1016/j.apenergy.2025.126185.

[11] Hensle N, Brinker D, Metz S, Smolinka T, Weber A. On the role of inductive loops at low frequencies in PEM electrolysis. Electrochem Commun Jan. 2023;155:107585. https://doi.org/10.1016/j.elecom.2023.107585.

[12] Brinker D, et al. Inductive loops in impedance spectra of PEM water electrolyzers. J Power Sources Dec. 2024;622:235375. https://doi.org/10.1016/j.jpowsour.2024.235375.

[13] Bernt M, Gasteiger HA. Influence of ionomer content in IrO2/TiO2 electrodes on PEM water electrolyzer performance. J Electrochem Soc Jan. 2016:3179–89.

[14] Briguglio N, et al. Design and testing of a compact PEM electrolyzer system. Int J Hydrogen Energy Jan. 2013;38(26). https://doi.org/10.1016/j.ijhydene.2013.04.091. Art. no. 26.

[15] Ferriday T, Middleton PH. Experimental analysis of materials in proton exchange membrane electrolysis cells. Int J Hydrogen Energy Jan. 2019;44(51). https://doi.org/10.1016/j.ijhydene.2019.09.020. Art. no. 51.

[16] Grigoriev SA, et al. Hydrogen safety aspects related to high-pressure polymer electrolyte membrane water electrolysis. Int J Hydrogen Energy Jan. 2009;34(14). https://doi.org/10.1016/j.ijhydene.2009.01.047. Art. no. 14.

[17] Grigoriev SA, Porembskiy VI, Korobtsev SV, Fateev VN, Auprêtre F, Millet P. High-pressure PEM water electrolysis and corresponding safety issues. Int J Hydrogen Energy Jan. 2011;36(3). https://doi.org/10.1016/j.ijhydene.2010.03.058. Art. no. 3.

[18] Hartig-Weiß A, Bernt M, Siebel A, Gasteiger HA. A platinum micro-reference electrode for impedance measurements in a PEM water electrolysis cell. J Electrochem Soc Jan. 2021;168(11). https://doi.org/10.1149/1945-7111/ac3717. Art. no. 11.

[19] Li N, Araya SS, Kær SK. Effect of current density, temperature and pressure on proton exchange membrane electrolyser stack. Int J Energy Power Eng Jan. 2021 15(1):15-18.

[20] Marangio F, Pagani M, Santarelli M, Calì M. Concept of a high pressure PEM electrolyser prototype. Int J Hydrogen Energy Jan. 2011;36(13). https://doi.org/10.1016/j.ijhydene.2011.01.091. Art. no. 13.

[21] Parra-Restrepo J, et al. Influence of the porous transport layer properties on the mass and charge transfer in a segmented PEM electrolyzer. Int J Hydrogen Energy Jan. 2020;45(15). https://doi.org/10.1016/j.ijhydene.2020.01.100. Art. no. 15.

[22] Santarelli M, Medina P, Calì M. Fitting regression model and experimental validation for a high-pressure PEM electrolyzer. Int J Hydrogen Energy Jan. 2009; 34(6). https://doi.org/10.1016/j.ijhydene.2008.11.036. Art. no. 6.

[23] Suermann M, Pătru A, Schmidt TJ, Büchi FN. High pressure polymer electrolyte water electrolysis: test bench development and electrochemical analysis. Int J Hydrogen Energy Jan. 2017;42(17). https://doi.org/10.1016/j.ijhydene.2017.01.224. Art. no. 17.

[24] Garcia-Navarro JC, Schulze M, Friedrich KA. Measuring and modeling mass transport losses in proton exchange membrane water electrolyzers using electrochemical impedance spectroscopy. J Power Sources Jan. 2019;431:189–204. https://doi.org/10.1016/j.jpowsour.2019.05.027.

[25] Klotz D, Weber A, Ivers-Tiffée E. Practical guidelines for reliable electrochemical characterization of solid oxide fuel cells. Electrochim Acta Jan. 2017;227:110–26. https://doi.org/10.1016/j.electacta.2016.12.148.

[26] Wang S, Zhang J, Gharbi O, Vivier V, Gao M, Orazem ME. Electrochemical impedance spectroscopy. Nat Rev Methods Primers Jan. 2021;1(1). https://doi.org/10.1038/s43586-021-00039-w. Art. no. 1.

[27] Orazem ME, Tribollet B. Electrochemical impedance spectroscopy. In: The electrochemical society series. second ed. Hoboken New Jersey: Wiley; 2017.

[28] Lasia A. Electrochemical impedance spectroscopy and its applications. New York, NY; Heidelberg: Springer; 2014 [Online]. Available: http://www.loc.gov/catdir/enhancements/fy1405/2013954801-b.html.

[29] Schönleber M, Klotz D, Ivers-Tiffée E. A method for improving the robustness of linear kramers-kronig validity tests. Electrochim Acta Jan. 2014;131:20–7. https://doi.org/10.1016/j.electacta.2014.01.034.

[30] Dierickx S, Weber A, Ivers-Tiffée E. How the distribution of relaxation times enhances complex equivalent circuit models for fuel cells. Electrochim Acta Jan. 2020;355:136764. https://doi.org/10.1016/j.electacta.2020.136764.

[31] Ivers-Tiffée E, Weber A. Evaluation of electrochemical impedance spectra by the distribution of relaxation times. J Ceram Soc Jpn Jan. 2017;(4):125. Art. no. 125 [4].

[32] Tikhonov AN, Gončarskij A, Stepanov VV, Jagola AG, editors. Numerical methods for the solution of ill-posed problems. Springer eBook collection mathematics and statistics, 328. Dordrecht: Springer; 1995. https://doi.org/10.1007/978-94-015-8480-7. vol. 328.

[33] Schiefer A, Heinzmann M, Weber A. Inductive low-frequency processes in PEMFC-Impedance spectra. Fuel Cells Jan. 2020;20(4). https://doi.org/10.1002/fuce.201900212. Art. no. 4.

[34] Weber A. Impedance analysis of porous electrode structures in batteries and fuel cells. TM - Tech Mess Jan. 2021;88(1). https://doi.org/10.1515/teme-2020-0084. Art. no. 1.

[35] Hensle N, Hoffmann J, Najafianashrafi Z, Smolinka T, Abel Chuang P-Y, Weber A. Understanding the use of carbon-based porous transport layers at the cathode in PEM water electrolysis. J Power Sources June 2025;642:236913. https://doi.org/10.1016/j.jpowsour.2025.236913.

[36] Martin A, et al. The effect of cell compression and cathode pressure on hydrogen crossover in PEM water electrolysis. J Electrochem Soc Jan. 2022;169(1). https://doi.org/10.1149/1945-7111/ac4459. Art. no. 1.

[37] Suermann M, Schmidt TJ, Büchi FN. Cell performance determining parameters in high pressure water electrolysis. Electrochim Acta Jan. 2016;211:989–97. https://doi.org/10.1016/j.electacta.2016.06.120.

[38] Lickert T, et al. On the influence of the anodic porous transport layer on PEM electrolysis performance at high current densities. Int J Hydrogen Energy Jan. 2020;45(11). https://doi.org/10.1016/j.ijhydene.2019.12.204. Art. no. 11.

[39] Hensle N, Lickert T, Winterholler N, Smolinka T, Weber A. Water starvation phenomena in a segmented along the channel PEM water electrolysis cell. J Power Sources Oct. 2025;654:237865. https://doi.org/10.1016/j.jpowsour.2025.237865.

[40] Franz T, Miličić T, Papakonstantinou G, Vidaković-Koch T, Sundmacher K. On the origin of low-frequency inductive loops in the impedance spectra of proton exchange membrane water electrolyzers. J Power Sources Nov. 2025;655:237981. https://doi.org/10.1016/j.jpowsour.2025.237981.